

## Article

# The Fracture Evolution Mechanism of Tunnels with Different Cross-Sections under Biaxial Loading

Lexin Jia <sup>1,2</sup>, Shili Qiu <sup>1,\*</sup>, Yu Cong <sup>3</sup> and Xiaoshan Wang <sup>3</sup>

<sup>1</sup> State Key Laboratory of Geomechanics and Geotechnical Engineering, Institute of Rock and Soil Mechanics, Chinese Academy of Sciences, Wuhan 430071, China

<sup>2</sup> University of Chinese Academy of Sciences, Beijing 100049, China

<sup>3</sup> School of Civil Engineering, Qingdao University of Technology 11 Fushun Road, Qingdao 266033, China

\* Correspondence: slqiu@whrsm.ac.cn

**Abstract:** Biaxial compression tests based on an elliptical tunnel were conducted to study the failure characteristics and the meso-crack evolution mechanism of tunnels with different cross-sections constructed in sandstone. The progressive crack propagation process around the elliptical tunnel was investigated using a real-time digital image correlation (DIC) system. Numerical simulations were performed on egg-shaped, U-shaped, and straight-walled arched tunnels based on the mesoscopic parameters of the elliptical tunnel and following the principle of an equal cross-sectional area. The meso-crack evolution and stress conditions of the four types of tunnels were compared. The results show that (1) fractures around an elliptical tunnel were mainly distributed at the end of the long axis and mainly induce slabbing failure, and the failure mode is similar to a V-shaped notch; (2) strain localization is an important characteristic of rock fracturing, which forebodes the initiation, propagation, and coalescence paths of macro-cracks; and (3) the peak loads of tunnels with egg-shaped, U-shaped, and straight-walled arched cross-sections are 98.76%, 97.56%, and 90.57% that of an elliptical cross-section. The elliptical cross-section shows the optimal bearing capacity.

**Keywords:** elliptical chamber; section shape; fracture evolution; DIC



**Citation:** Jia, L.; Qiu, S.; Cong, Y.; Wang, X. The Fracture Evolution Mechanism of Tunnels with Different Cross-Sections under Biaxial Loading. *Processes* **2024**, *12*, 891. <https://doi.org/10.3390/pr12050891>

Academic Editor: Carlos Sierra Fernández

Received: 7 March 2024

Revised: 22 April 2024

Accepted: 25 April 2024

Published: 28 April 2024



**Copyright:** © 2024 by the authors. Licensee MDPI, Basel, Switzerland. This article is an open access article distributed under the terms and conditions of the Creative Commons Attribution (CC BY) license (<https://creativecommons.org/licenses/by/4.0/>).

## 1. Introduction

During the construction of deep tunnels, tunnel excavation frequently results in spalling and board cracking. In the event of high-stress conditions, rock burst damage can even occur, presenting significant challenges to the tunnel construction, support, and long-term stability [1–4]. In underground engineering, tunnels are typically circular or straight-walled arched [3,5–7]. However, during the construction process, various shapes may emerge for tunnels such as traffic tunnels, connecting tunnels, and water curtain tunnels, owing to the different construction methods employed. The shape of the tunnel section is a critical factor affecting the stability of the surrounding rock [8]. The process of tunnel excavation results in gradual brittle failure, which typically manifests as the formation of a V-shaped notch [1,3,9,10]. An understanding of the processes involved in the initiation and propagation of cracks in rock masses during tunnel excavation is beneficial to the evaluation of engineering stability and the design of tunnel support systems.

Laboratory mechanical and model experiments are commonly used and effective means of studying rock mass failure in tunnels. True triaxial experiments can well simulate the mechanical conditions of underground rock masses, typically using cubes to simulate the fracture characteristics of rock [11]. Through true triaxial tests on cube specimens, Wang [12] obtained that the rock burst tendency of hard rock is related to the strength parameters and brittleness index of rock materials. Lu [13] used the true triaxial one-sided unloading test on rock samples and pointed out that with the increase in the intermediate principal stress, the strength of the sample first increased and then decreased, and the V-shape was approximately parallel to the intermediate principal stress. Through the true

triaxial loading and unloading tests of granite, red sandstone, and cement mortar, Du [14] studied the failure mechanical behavior of different rock types under the unloading path and pointed out that the granite and red sandstone exhibited obvious slabbing failure after unloading, and the cement mortar sample showed shear failure. The above research mainly simulated tunnel failure from the perspective of material failure and stress paths, without considering the influence of tunnel structure failure. Some scholars have used specimens with prefabricated holes for experimental simulations. For example, Gong [6,7] conducted loading tests on cubic sandstone samples with circular holes under three-dimensional stress at varying depths. Their research focused on the rock burst process caused by spalling. The hole has a strength size effect on the sidewall damage due to the limitations of the size of the test sample. Mei [15] established a large-scale model through 3D-printing technology and conducted excavation and multi-stage loading tests, which revealed that tensile damage was primarily observed during excavation, and shear damage was primarily observed during multi-stage loading tests. However, it is important to note that there are some differences between the mechanical properties of similar materials and rocks. Therefore, it is necessary to carry out large-scale loading tests with real rock samples while considering the shape of the tunnel.

Crack initiation and propagation in a rock mass controls the mechanical behavior and failure mechanism of the rock, and it is an important part of studying the evolution process of rock fracture [16]. In previous tests, a high-speed camera was employed to observe and record the propagation and failure mode of rock cracks. Consequently, the identification of cracks relies on the naked eye to discern the macro-crack growth trend through the observation of images [17–19]. It is evident that cracks can only be observed when the specimen exhibits clear slip, fracture, and other behaviors, which may result in erroneous judgments regarding the crack initiation time and position. Moreover, the data obtained are only qualitative and not quantitative. Digital image correlation is a measurement technique that can be used to monitor crack initiation and propagation [20]. A multitude of tests have demonstrated that DIC technology is an effective means of characterizing the fracture and crack propagation of rock masses [21–25]. According to different crack mechanisms, the crack types can be divided into tensile crack, shear crack, and tensile–shear crack [26]. Zhou [27] conducted a failure study on marble specimens with rectangular cavities under uniaxial loading, and the main failure modes were splitting failure, shear failure, mixed tensile/shear failure, and surface spalling. The characteristics of crack growth are also influenced by the confining pressure and unloading rate. Specifically, the crack growth rate exhibits an inverse relationship with the confining pressure and direct proportionality with the unloading rate [28].

This study employed engineering rock sandstone as the experimental research object. The cube sample was equipped with elliptical holes and subjected to in situ stress environments. The axially graded loading method was employed to destroy the tunnel, and a high-speed camera was utilized to record and monitor the process in real time, with subsequent DIC analysis. Based on the experimental results, a discrete element model was constructed to analyze the tunnel fracture process from a mesoscopic perspective. The calculation and analysis of different section shapes were carried out while maintaining the same section area, which facilitated the optimization of the engineering support and excavation schemes.

## 2. Biaxial Compression Tests on an Elliptical Tunnel Sample

### 2.1. Model Preparation

A large natural sandstone block was excavated from an underground tunnel, which was machined into a single-tunnel model measuring 500 mm × 500 mm × 100 mm (length × width × thickness) in a stone factory. The surface evenness of the machined rock sample was 0.5 mm. An elliptical hole through the sample was drilled in the model by using a water-jet scalpel, with the long and short axes of the ellipse being 110 and 95 mm, respectively [29,30]. The prototype and model of the tunnel are shown in Figure 1.

The standard cylindrical sandstone specimen had the following mechanical parameters: a uniaxial compressive strength of 43 MPa, a modulus of elasticity of 10.1 GPa, a density of 2120 kg/m<sup>3</sup>, and a wave velocity of 2940 m/s.

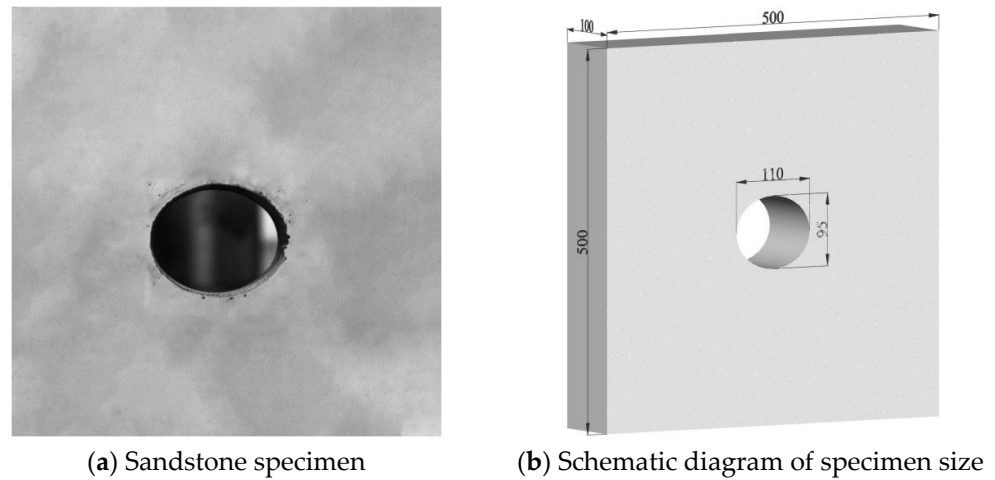


**Figure 1.** Tunnel prototype and model (unit: mm).

## 2.2. DIC Technique

Digital image correlation (DIC) is a non-contact and non-destructive optical technique used to measure the surface deformation of a specimen. This is achieved by comparing successive images of the specimen surface to extract deformation and displacement data. The core of DIC involves calculating surface strain by analyzing pixel displacement differences across images. The basic principle of a DIC test is to capture grayscale images at various intervals during the experiment. Then, the region of interest (ROI) within the specimen is defined, and the distances between different monitoring points are determined. An array of these points is created, and appropriate correlation functions and displacement patterns are selected for pixel matching. Pre-deformation and post-deformation assessments of the ROI are performed. The selection of a correlation function is crucial in this process. To improve surface features, scattering spots are often introduced during experimental tests. These spots can take on various forms, including natural and artificially prefabricated ones. However, natural scattering spots often do not meet the calculation requirements for most experimental objects, so various artificial fabrication techniques are used. These methods include black and white paint spraying, dot painting with marking pens, and using scattering spot stickers. Digital image correlation technology focuses on matching pixel points. A single pixel point with discrete matching is often insufficient, so the pixel features of the monitoring point and its specific surrounding area are needed for localization. The image of the area produced with the monitoring point as the center when it is not deformed before the test is known as the reference sub-area, and the area after the deformation occurs is known as the target sub-area. The matching problem for pixel points is transformed into a matching problem for the entire subregion, and selecting appropriate correlation functions is necessary to ensure accurate subregion matching. The zero-normalized sum of squared differences (ZNSSD) is used as the correlation function to obtain an accurate characterization of the deformation [31]:

$$C_{ZNCCD} = \sum_{i=-M}^M \sum_{j=-M}^M \left[ \frac{f(x_i, y_j) - f_m}{\sqrt{\sum_{i=-M}^M \sum_{j=-M}^M [f(x_i, y_j) - f_m]^2}} - \frac{g(x_i, y_j) - g_m}{\sqrt{\sum_{i=-M}^M \sum_{j=-M}^M [g(x_i, y_j) - g_m]^2}} \right] \quad (1)$$

where  $M$  is the radius of the sub-region, and  $f(x_i, y_j)$  and  $g(x_i, y_j)$  are the pixel value functions at the coordinates of the pixel points in the reference and deformed regions.  $f_m$  and  $g_m$  are the average values of a subset of pixels in the region before and after deformation, respectively:

$$f_m = \frac{1}{(2M + 1)^2} \sum_{i=-M}^M \sum_{j=-M}^M f(x_i, y_j) \quad (2)$$

$$g_m = \frac{1}{(2M + 1)^2} \sum_{i=-M}^M \sum_{j=-M}^M g(x_i, y_j) \quad (3)$$

where  $(2M + 1)^2$  is the area of the region. Through the above formula, the ZNSSD function of the value of the domain of  $[0, 4]$  can be obtained, so the ZNSSD function of the test process of the influence of the change in the light source, the camera's own noise impact, and other cases have strong applicability.

It is important to note that the standard DIC technique is based on the assumption of deformation continuity. Consequently, the calculated results are subject to significant errors when the surface contains discontinuous media points [31,32]. Therefore, when performing strain field calculations, it is necessary to subtract the prefabricated hole region.

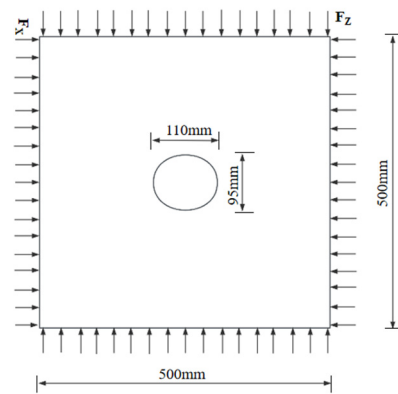
### 2.3. Loading Devices and Schemes

The biaxial compression tests on the sandstone with an elliptical tunnel were carried out on a TATW-2000 triaxial testing machine for rocks, which could monitor the load and deformation in real time during the test. Steel pressing plates were placed on the left and right sides of the model, and they were connected with hydraulic pumps through which the confining pressure was applied. To ensure uniform stress on the model, a steel pressing plate was separately put on the top and bottom of the model. To reduce the influence of friction on the test results, a layer of Vaseline™ was smeared onto the four side faces (the top, bottom, left, and right faces) of the tunnel. The center of the vertical loading cylinder of the testing machine and the tunnel center were on the same perpendicular line so as to avoid eccentric compression. The loading of the tunnel model and the loading devices are illustrated in Figure 2. Before the experiment, the sample surface was painted with black and white paint to create a random speckle pattern with a speckle diameter of about 2 mm for the digital image correlation (DIC) analysis. During the test, a high-speed camera was placed in front of the model to record the deformation of the surface of each shelter. The images were captured at a rate of 5 frames per second, with a resolution of 1616 pixels by 1682 pixels and an acquisition range of 10 cm by 10 cm around the hole perimeter.

The horizontal in situ stress at the site where the rock sample was collected was 2.1 to 3.0 MPa, so the horizontal maximum stress in the tests was designed to be 3 MPa. As the tunnel excavation progressed, the stress on the surrounding rock of the tunnel gradually increased. Consequently, the stress paths employed a multiple-stage loading method, which was maintained for a specified period following each level of loading. To ascertain the ultimate bearing capacity of the test model, three samples were extracted from the same batch, and the mean value was calculated. The ultimate vertical load that could be borne by the tunnel constructed in heavily weathered sandstone was about 1000 kN.

The stress paths in the biaxial loading tests on the tunnel model are shown in Figure 3. A pre-pressure of 2 kN was vertically applied to ensure the complete tight contact of the pressure head of the testing machine with the upper surface of the single-tunnel model. A hydraulic pump was adopted to apply a confining pressure of 3 MPa to the tunnel model in the horizontal direction, which remained unchanged throughout the test. The vertical load was applied in multiple stages (the vertical load was first increased to 450 kN at a rate of 500 N/s in the stress-controlled mode, held for 200 s, and then increased by 100 kN in each stage at a rate of 0.02 mm/min in the displacement-controlled mode, followed by 300 s of holding after loading at each stage; this process was repeated until the failure of

the tunnel). In the test process, test data including the load, deformation, and DIC data in the whole failure process of the elliptical tunnel were recorded synchronously.



(a) Demonstration of rock sample loading (b) Rock triaxial testing machine

**Figure 2.** Model forcing demonstration and loading device.

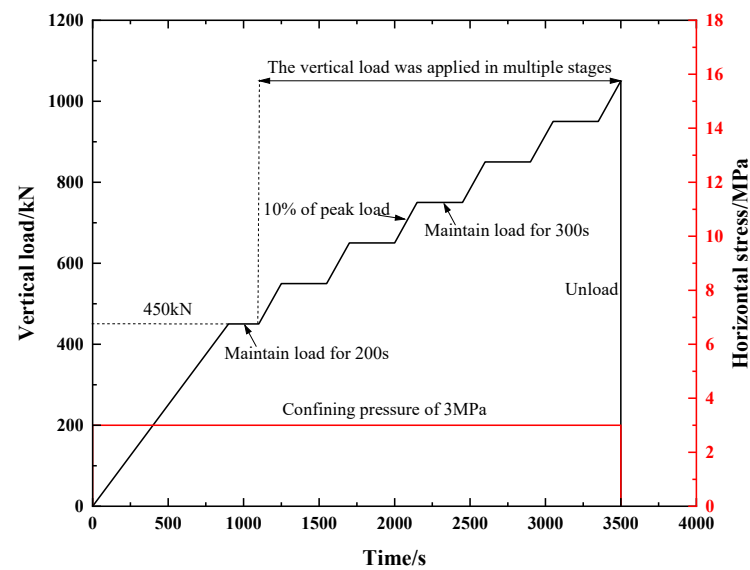


**Figure 3.** Stress paths in tunnel biaxial loading tests.

### 3. Crack Propagation and Strain Field Evolution Characteristics of the Tunnel

#### 3.1. Evolution of Surface Macro-Cracks

##### 3.1.1. Macro-Crack Evolution

The evolution of macro-cracks and strain fields on the tunnel surface is illustrated in Figure 4 (serial numbers 1 to 8 indicate the crack initiation sequence). The solid and dotted lines separately represent the outlines of the cracks and bulging of the surface rock slabs, and the crack angle indicates the angle between a crack and the horizontal direction.

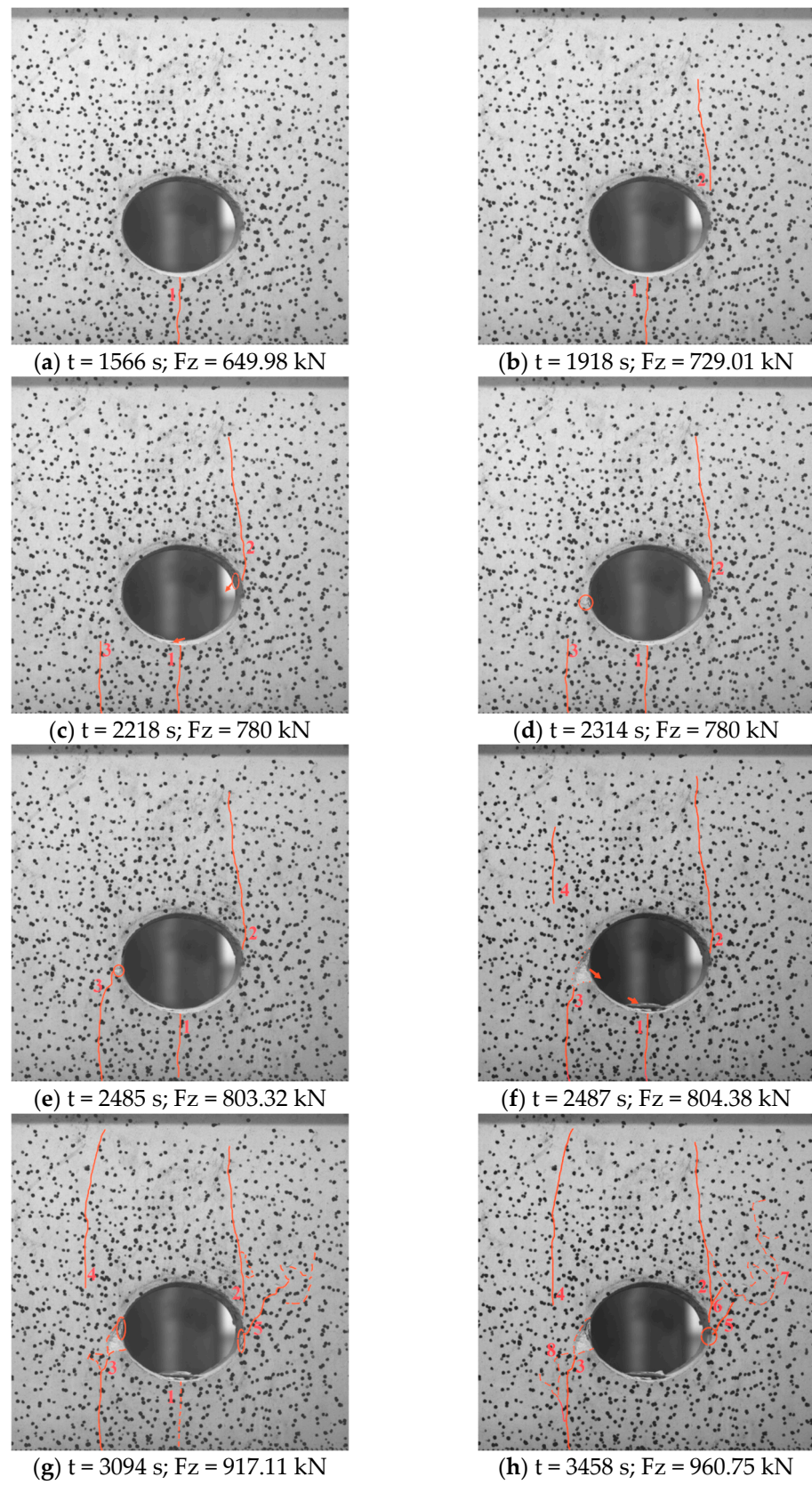
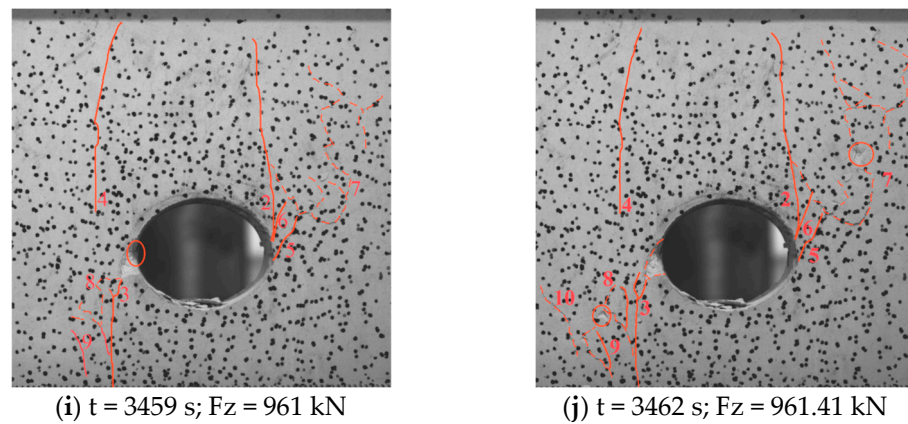


Figure 4. Cont.



**Figure 4.** Crack evolution of tunnel. (Serial numbers 1 to 8 indicate the crack initiation sequence; the solid and dotted lines separately represent the outlines of cracks and bulging of surface rock slabs).

- (1) When loading to  $t = 1566$  s ( $F_z = 649.98$  kN), a vertical crack 1 with a length of 60 mm appears just below the bottom of the tunnel entrance, which is a tension crack, as shown in Figure 4a.
- (2) At  $1566 < t \leq 1918$  s ( $649.98 < F_z \leq 729.01$  kN), crack 1 does not change to any apparent extent and crack 2 with a length of 120 mm that vertically propagates upwards is initiated at a position of 20 mm from the spandrel in the upper right part of the tunnel entrance, as displayed in Figure 4a,b.
- (3) At  $1918 < t \leq 2218$  s ( $729.01 < F_z \leq 780$  kN), crack 1 does not change to any apparent extent. The lower tip of crack 2 propagates, and the upper tip develops approximately vertically upwards to 140 mm (this is accompanied by the ejection of fine rock blocks from the right-hand wall of the tunnel). At that time, the tunnel is initially damaged, and a vertical shearing crack 3 with a length of 60 mm lying parallel to crack 1 is initiated in the lower left part of the tunnel, as displayed in Figure 4b,c.
- (4) At  $2485 < t \leq 2487$  s ( $803.32 < F_z \leq 804.38$  kN), crack 1 does not show any obvious change; crack 2 continues to develop upwards to 150 mm; and crack 3 propagates and coalesces with tiny cracks at the left haunch of the tunnel entrance, which cuts the surface rock and triggers the exfoliation thereof. The flake-like rocks slide from the left-side wall to the bottom of the tunnel under the action of the stress on the inner wall of the tunnel and gravity. Meanwhile, crack 4, with a length of 60 mm, propagates vertically upwards, appearing in the upper left part of the entrance, as shown in Figure 4e,f.
- (5) At  $2487 < t \leq 3094$  s ( $804.38 < F_z \leq 917.11$  kN), crack 1 narrows and tends to close; crack 2 does not change to any obvious extent; a micro-crack appears and the rock slightly bulges to the left side of the upper tip of crack 3; crack 4 continues to develop vertically upwards to 140 mm; crack 5 appears at the right haunch, which develops obliquely ( $60^\circ$ ) to the upper right part; and the rock near the upper tip of crack 5 bulges slightly. At the same time, the left- and right-side walls show slabbing characterized by tilted rocks, and the blocks tend to be exfoliated, as displayed in Figure 4f,g.
- (6) At  $3094 < t \leq 3458$  s ( $917.11 < F_z \leq 960.75$  kN), crack 1 is completely closed; cracks 2 and 4 do not change to any obvious extent; crack 3 also undergoes no apparent change, while the surface rock to the left side bulges slightly (marked as 8 in Figure 4h); particles are ejected at the location where crack 5 coalesces with the tunnel wall; a new crack 6 with a length of 30 mm appears at the lower tip of crack 2; and, meanwhile, the zone of bulging of the rock in the upper right part of the tunnel is enlarged, albeit the bulging itself remains slight (marked as 7 in Figure 4h), as illustrated in Figure 4g,h.
- (7) At  $3058 < t \leq 3459$  s ( $960.75 < F_z \leq 961$  kN), the lengths of the surface macro-cracks on the tunnel do not change to any apparent extent, and the bulging rocks at the left haunch of the entrance are exfoliated; crack 9 with a length of 40 mm is initiated to

the left of crack 3, and it inclines by  $110^\circ$  toward the upper left part; and the surface rocks on the tunnel bulge are more obviously (marked as 7 and 8 in Figure 4h), as displayed in Figure 4h,i.

- (8) At  $3059 < t \leq 3462$  s ( $961 < Fz \leq 961.41$  kN), the surface cracks of the tunnel do not change to any apparent extent; as loading continues, new slabbing and exfoliation occur alternately on the left and right sides of the tunnel; and surface rocks on the tunnel continue to bulge (marked as 7, 8, and 10 in Figure 4h), with rock exfoliation seen above crack 7 and below crack 8, leading to the severe brittle failure of the tunnel and a popping sound, as shown in Figure 4i,j.

There are three types of cracks that occur during tunnel loading. (1) Tension cracks: Tension cracks formed in the tensile stress concentration area around the tunnel during the loading process are initial cracks. (2) Shear cracks: Shear cracks formed by compressive stress concentration near the tunnel are the main destructive cracks. (3) Tensile–shear cracks: Tensile–shear cracks are mainly distributed in the far field of the tunnel, formed at the far end of the tunnel perimeter. Accordingly, the cracks on the surface of the tunnel are identified as follows: cracks 1 and 2, which were formed at the stage of crack initiation and appeared at the top and bottom of the tunnel arch, belong to tensile cracks; cracks 3, 4, 6, and 7, which were caused by compressive stress concentration and formed at the waist of the tunnel arches, belong to shear cracks; and cracks 5 and 8, which were formed at the distal end of the tunnel, belong to far-field cracks.

### 3.1.2. Macro-Failure Modes

The failure modes of the inner walls of the elliptical tunnel are displayed in Figure 5. The interior shows slabbing-dominated failure, and failure has coalesced on the left side wall along the depth direction of the tunnel, similar to a V-shaped notch. Many exfoliated blocks and much debris are observed on the bottom of the tunnel, the central thickness of which is about 3 to 5 mm. In the meantime, some fractured blocks remain, un-ejected, on the tunnel walls.

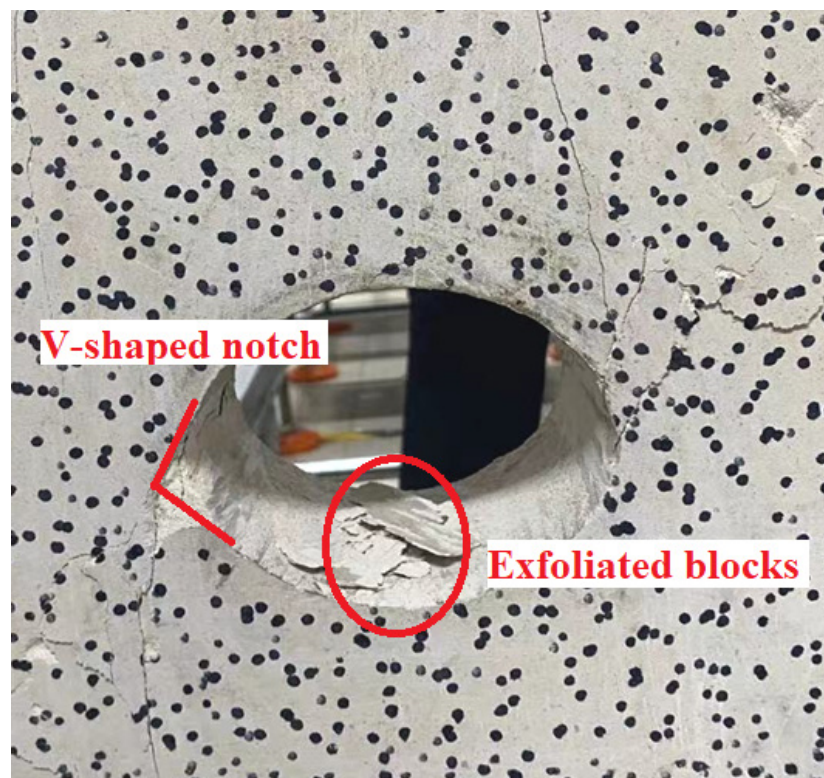


Figure 5. Wall damage inside of elliptical tunnel.

In summary, the ejection of small particles, slabbing, and the exfoliation of rock blocks arose in the elliptical tunnel over the whole loading process. Theoretically, these phenomena should be symmetrical and synchronized on the left- and right-side walls of the tunnel, while, in fact, the left- and right-side walls of the elliptical tunnel are not damaged synchronously. The left wall remains relatively intact during the exfoliation of the right-side wall, which is due to influences of the anisotropy of the sandstone itself and the machining precision of the sample.

### 3.2. Strain Field Evolution

A high-speed camera was used to acquire images during the whole deformation process of the single tunnel, and the change process in the strain field on the surface of the tunnel processed by Vic-2D software (<https://www.correlatedsolutions.com/vic-2d>, 24 April 2024) is shown in Figure 6.

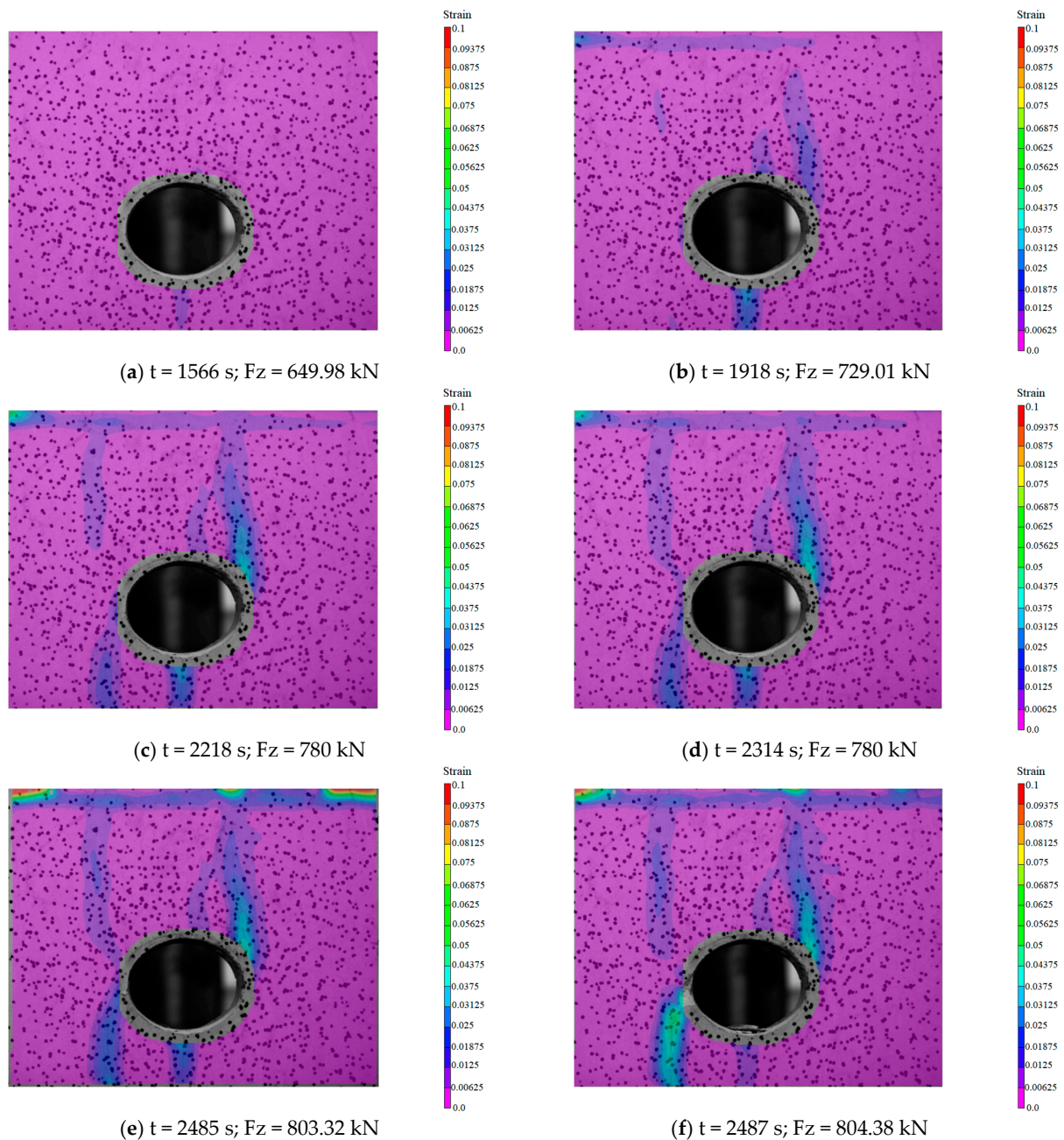
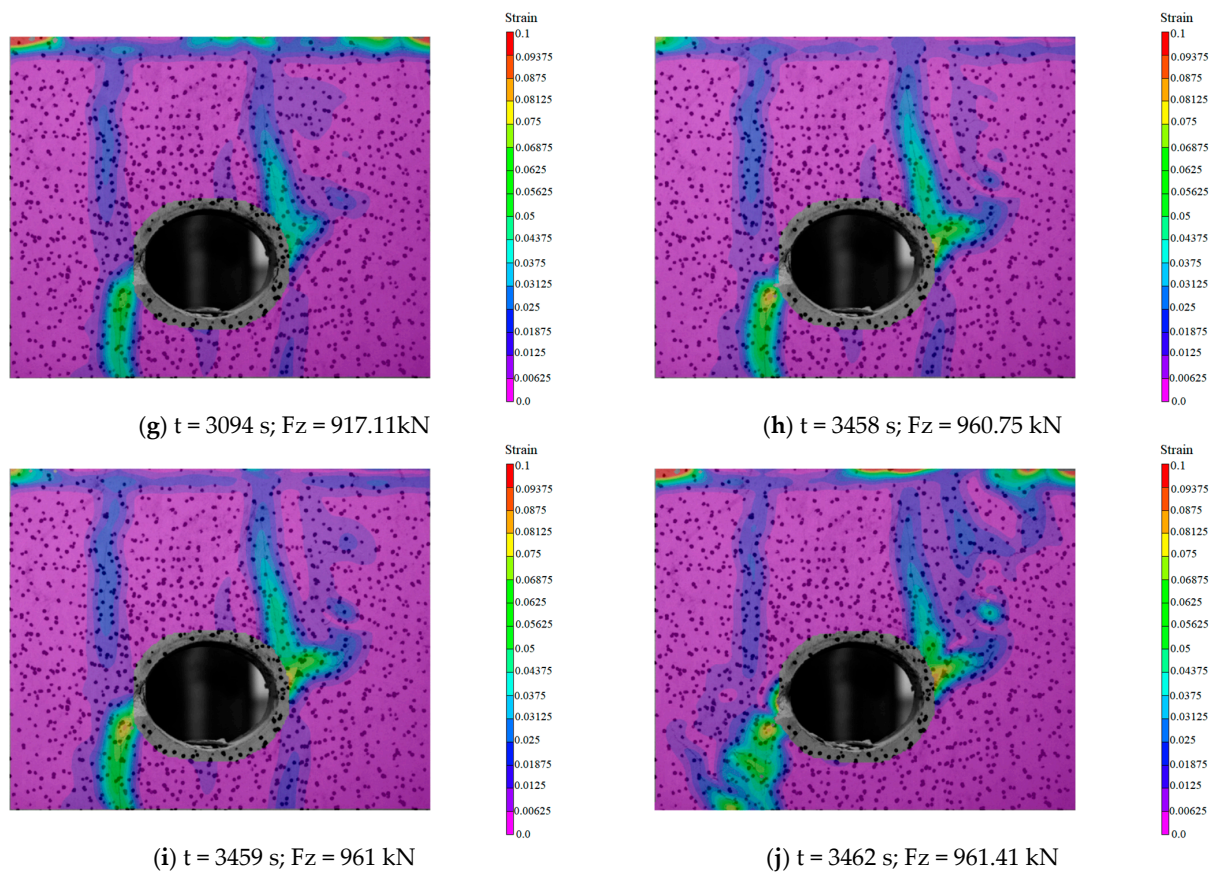


Figure 6. Cont.



**Figure 6.** Strain field evolution process under biaxial loading ( $t$  is the loading time;  $F_z$  is the axial force).

- (1) When loading to  $t = 1566$  s ( $F_z = 649.98$  kN), an elliptical stress concentration zone appears just below the invert of the tunnel (Figure 6a), in which the maximum strain is 0.005, while the strain in other areas is low (0 to 0.0025). The comparison with Figure 6a shows that a vertical crack appears here.
- (2) At  $1566 < t \leq 1918$  s ( $649.98 < F_z \leq 729.01$  kN), as displayed in Figure 6a,b, the strain concentration zone below the invert is widened, in which the maximum strain is increased to 0.0125; a vertical strain concentration zone appears at the right spandrel of the tunnel, in which the maximum strain is 0.0075; and strain concentration zones are also seen above the vault and the upper left part of the tunnel, in which the strain is relatively low (0.0025 to 0.005), which indicates crack initiation thereat. The comparison with Figure 4a,b reveals that a vertical crack is initiated at the right spandrel of the tunnel.
- (3) At  $1918 < t \leq 2218$  s ( $729.01 < F_z \leq 780$  kN), the strain concentration zone below the invert does not vary to any apparent extent (Figure 6b,c); the strain concentration zone above the vault develops obliquely to the upper right part and coalesces with the strain concentration zone at the spandrel, where the strain remains low (0.005); the strain concentration zone at the right spandrel develops upwards and its width increases, in which the maximum strain increases to 0.015; the strain concentration zone in the upper left part of the tunnel extends vertically upwards, while the strain is low (0.005); and a new vertical strain concentration zone appears in the lower left part, in which the maximum strain is 0.0075. The comparison with Figure 4b,c shows that a new vertical crack is initiated in the lower left part of the tunnel.
- (4) At  $2485 < t < 2487$  s ( $803.32 < F_z \leq 804.38$  kN), the strain concentration zone above the vault of the tunnel does not change to any apparent extent (Figure 6e,f); the range of the strain concentration zone below the invert does not vary, while the maximum strain decreases to 0.005; the range of the strain concentration zone at the

right spandrel does not expand while the strain increases, with the maximum value being 0.02; the strain concentration zone below the lower left part of the tunnel is widened, while the strain significantly increases, with the maximum value being 0.02; and the strain concentration zone in the upper left part of the tunnel shortens, while the strain increases to 0.008. The comparison with Figure 4e,f shows that the crack in the upper right part of the tunnel develops upwards; the crack length below the invert does not change; a small rock block is exfoliated from the left haunch; and a new crack is initiated in the upper left part of the tunnel.

- (5) At  $2487 < t \leq 3094$  s ( $804.38 < Fz \leq 917.11$  kN), the strain concentration zones at the invert and vault of the tunnel do not change to any apparent extent (Figure 6f,g); the strain concentration zone at the right haunch extends rightwards, in which the maximum strain is between 0.0175 and 0.0225; the strain concentration zone in the left lower part is widened, in which the maximum strain increases to 0.03; and the strain concentration zone in the upper left part propagates vertically downwards, in which the strain increases to 0.01 to 0.0125. The comparison with Figure 4e,f shows that the crack in the upper left part develops upwards, and surface rocks in some areas of the tunnel bulge.
- (6) At  $3094 < t \leq 3458$  s ( $917.11 < Fz \leq 960.75$  kN), Figure 6g,h demonstrates that the ranges of strain concentration zones in the upper right and lower left parts of the tunnel increase, heralding the possibility of tiny cracks occurring in these zones, while other strain concentration zones do not change to any apparent extent. The comparison with Figure 4g,h reveals that the cracks do not continue to propagate until stress equilibrium is restored-
- (7) At  $3058 < t \leq 3462$  s ( $960.75 < Fz \leq 961.41$  kN), the strain concentration zone in the upper left part of the tunnel changes slightly. Strain concentration zones mainly appear at the left haunch and below the arch foot of the elliptical entrance, as well as at the right haunch and the upper part, in which the maximum strain increases to 0.035 (Figure 6h-j). The comparison with Figure 4h,j shows that cracks propagate and coalesce, and the tunnel undergoes brittle failure.

Analysis of the strain field evolution around the elliptical tunnel constructed in sandstone under biaxial compression reveals that the positions of strain concentration zones on the tunnel surface correspond to the crack initiation and propagation positions. Therefore, strain localization is an important characteristic of rock fracturing, which is manifest in the non-uniform distribution of local strain on the tunnel surface. It forebodes the initiation, propagation, and coalescence of macro-cracks.

### 3.3. Evolution of Effective Variance

The root cause of the deformation localization of rock is the development process of its internal crack. The effective variance statistical index of the strain field represents the non-uniform evolution process of the single cave surface strain field. Therefore, the effective variance index of the strain field is related to the evolution of the crack in the rock. Covariance is employed to assess the overall discrepancy between two variables. In contrast, a covariance matrix is utilized to quantify the overall discrepancy among multiple components, with each element representing the covariance between multiple components. This study employed the effective variance of the stress field to investigate the variation in the strain fields in rock-like specimens [33]. It also explored the evolution pattern of the effective variance of strain fields during the deformation and failure process of a single tunnel. The DIC technology was employed to obtain the horizontal strain field, vertical strain field, and shear strain field data during the loading damage process in a single hole. These data were imported into MATLAB to calculate the covariance matrix of the three strain components, and then the arithmetic square root was calculated to obtain the effective variance of the strain field. The strain tensor  $\mathbf{S}$  and strain vector are:

$$\mathbf{S} = \begin{bmatrix} \varepsilon_{xx} & \varepsilon_{xy} \\ \text{symmetric} & \varepsilon_{yy} \end{bmatrix} \quad (4)$$

$$\mathbf{S}_d = \text{vech}(\mathbf{S}) = [\varepsilon_{xx} \ \varepsilon_{xy} \ \varepsilon_{yy}]^T \quad (5)$$

where  $\text{vech}(\mathbf{S})$  is the half-angle vectorization operator.

The mean vector  $\overline{\mathbf{S}}_d$  is:

$$\overline{\mathbf{S}}_d = \frac{1}{n} \sum_{i=1}^n \mathbf{S}_{d_i} \quad (6)$$

Then, the covariance matrix  $\Omega$  of the strain component is:

$$\Omega = \text{cov}(\mathbf{S}_d) = \frac{1}{n} \sum_{i=1}^n (\mathbf{S}_{d_i} - \overline{\mathbf{S}}_d) \cdot (\mathbf{S}_{d_i} - \overline{\mathbf{S}}_d)^T \quad (7)$$

where  $n$  is the total number of data for the strain component, and  $\mathbf{S}_{d_i}$  is the strain vector for the  $i$ -th set of data.

The effective variance of the strain field is ultimately defined as:

$$V_e = \frac{1}{2} p(p+1) \sqrt{|\Omega|} \quad (8)$$

where  $p$  is the tensor dimension.

The effective variance curves of the strain field in the loading process of the elliptical tunnel were obtained, as shown in Figure 7, which shows obvious stages. At the beginning of loading, the effective variance of the strain field is close to zero. This is due to the uniform distribution of the strain field, and the values of the horizontal, vertical, and shear strains are close to each other, with no obvious differentiation. When loaded to point A, a tensile crack appears below the bottom of the single refuge arch (Figure 8a,b), forming a strain concentration zone, the effective variance shows a slow increase in the law of change. As the vertical load increases, the effective variance increases steeply at point B. The degree of divergence of the strain field suddenly increases, and the number of macroscopic cracks on the surface of the single refuge increases, accompanied by the spalling of the rock mass, as shown in Figure 8c,d. Until point C is reached, the strain field increases, but the location of the strain concentration does not change much, and the cracks on the surface of the single refuge continue to expand, with a slow increase in the effective variance. When the peak stress of the single refuge is reached (point C in Figure 7), the effective variance of the strain field suddenly increases dramatically, the strain values deviate from the mean to a significant extent, and the cracks on the surface of the single refuge and the corresponding strain concentration zones expand rapidly through the whole specimen (Figure 8e,f).

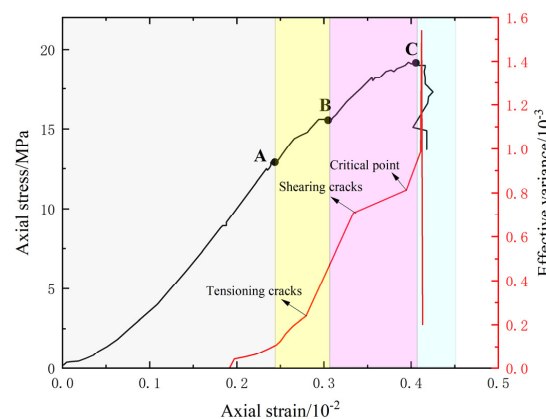


**Figure 7.** Stress and effective variance versus strain relationship curves. (point A, B, C is the demarcation point of each stage).

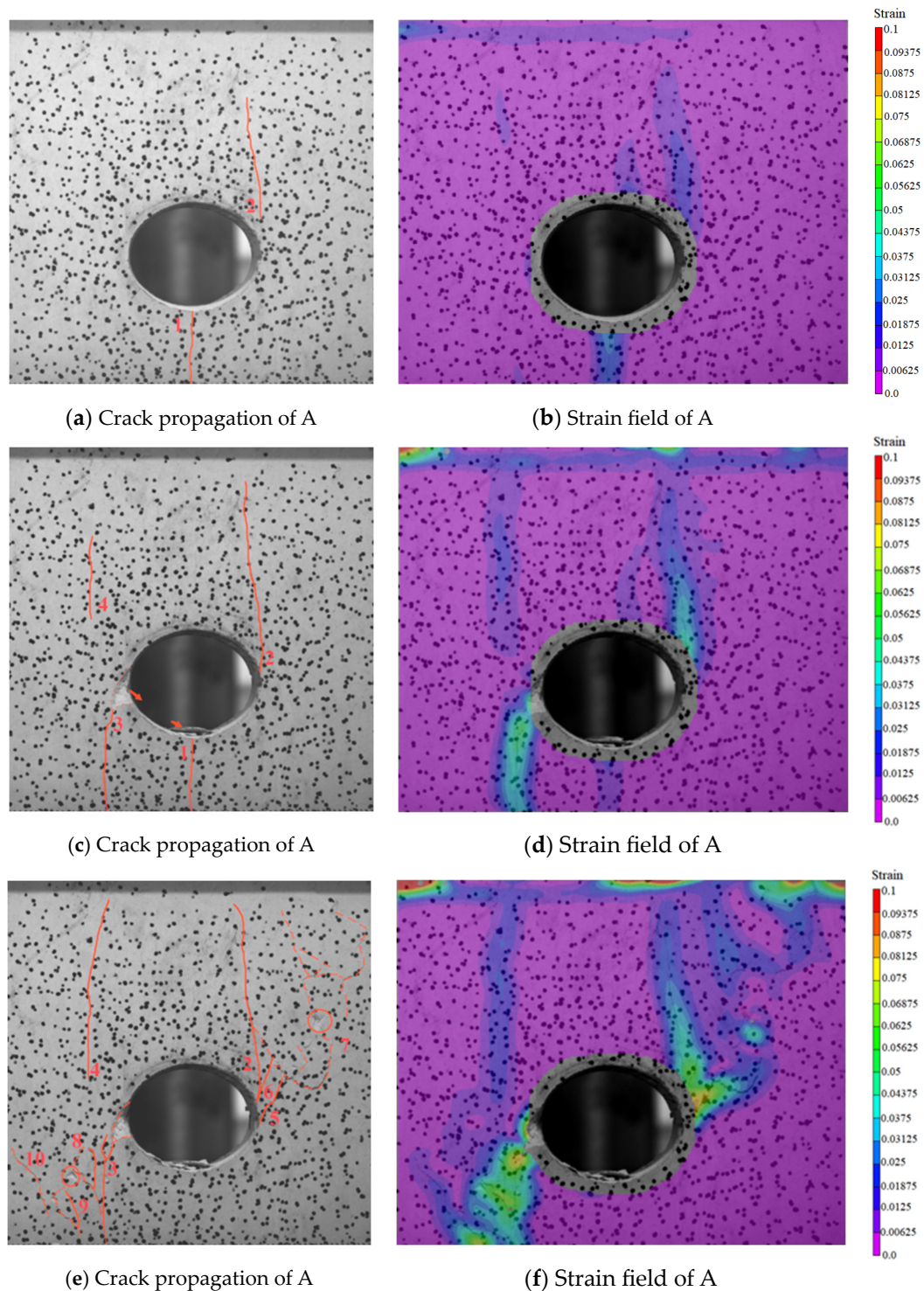


**Figure 8.** Characteristic point crack propagation and strain field. (serial numbers 1 to 10 indicate the crack initiation sequence; the solid and dotted lines separately represent the outlines of cracks and bulging of surface rock slabs; the dots are scattered dots).

#### 4. PFC Simulations of Failure Tests of the Tunnel

##### 4.1. PFC Simulations and Mesoscopic Parameters

Laboratory tests mainly explore the macroscopic failure characteristics of tunnels, while they fail to reveal the mesoscopic mechanical properties. By using the discrete element software particle flow code (PFC2D) (<https://itascasoftware.com/products/pfc2d/>, 24 April 2024), numerical simulations of the failure tests of the similarity model of the elliptical

tunnel constructed in sandstone were conducted. In the discrete element program, discrete particles are allowed to move or rotate freely. Since these particles are rigid bodies, their motion is described by both the translational velocity of the center of mass and the angular velocity of rotation. During the system calculation, the dynamic relaxation method is employed to solve the motion equations. For each discrete node, the second-order central difference method is utilized to update its displacement while accounting for mass damping. Since rigid particles cannot undergo deformation, interactions between particles are solved by establishing contacts between them. When particles come into contact with each other or with boundaries such as walls, a contact model is established at the surface connection of each particle. Interaction forces are transmitted through a system of normal and tangential springs and dampers. The parallel bond model was chosen for the constitutive model of the contact unit. After the parallel bond is established, the relative motion at the contact causes forces and moments to be generated within the bonded material, which is related to the maximum normal and shear stresses acting within the bonded peripheral material, and if any of these maximum stresses exceeds its corresponding bond strength, the parallel bond will fracture, and the accompanying forces and moments are removed from the model.

The mesoscopic parameters of the parallel bond model were adjusted to render the mechanical properties of the material used in the simulations to be as consistent with sandstone as possible. Then, a numerical model showing the equal dimension scale with the similarity model was established and damaged under overloads. The change trends of the parameters including the meso-fractures and main force chains in the failure process were obtained through programming, and then phenomena observed in the macroscopic tests were compensated and explained from the mesoscopic perspective.

The control variable method was used to estimate the influences of the mesoscopic parameters of the parallel bond model and those of the material itself on the overall macroscopic mechanical properties of the model. The laws or trends of the macroscopic and mesoscopic parameters' influences on each other were obtained, and the numerical model was damaged under loading. When characteristics including the overall compressive strength and surface crack distribution characteristics of the model tend to coincide with the test results of the elliptical tunnel model prepared using sandstone in Section 2, it means that this group of PFC mesoscopic parameters can reproduce the macroscopic mechanical properties of sandstone. The PFC mesoscopic parameters were finally determined through multiple adjustments (Table 1).

**Table 1.** Fine-scale parameters of particle flow.

Elastic Modulus/GPa	Porosity	Density/kg·m <sup>-3</sup>	Stiffness Ratio	Tensile Strength/MPa	Cohesion/MPa	Internal Friction Angle/°
35	0.16	2119	2.0	6	7.5	30

The PFC procedure is displayed in Figure 9. Quadrilateral walls measuring 500 mm × 500 mm were generated in the computation domain as the boundaries of the sample (Figure 9a). Random seeds were set to produce a total of 13,861 rigid spheres with a particle size of 4 to 5 mm in the walls. The contact stiffness model was used for both particle–particle and particle–wall contacts (Figure 9b) so that the computation could converge rapidly and particles were uniformly dispersed and stably stressed. Afterward, the parallel bond model was used for the particle–particle contact to simulate rock-like materials, while the contact stiffness model was still used for the particle–wall contact. Values were assigned to the mesoscopic parameters of contact elements in the parallel bond model, which was then solved and stabilized (Figure 9c). Before excavating the tunnel, a confining pressure of 3 MPa was applied uniformly to the four sides of the model using the servo-motor mechanism until the convergence of the computation so as to simulate the influence of the initial in situ stress (Figure 9d). An elliptical wall was generated in the center of the model and particles in the range of the wall to simulate the excavation process (Figure 9e). In the

excavation process, a constant horizontal pressure of 3 MPa was maintained on the left- and right-side walls by using the servo-motor mechanism. The displacement constraint was applied to the upper and lower sides of the model. The wall of the tunnel was deleted after excavation, and a speed of 0.002 mm/min was assigned to the upper and lower rigid walls to realize displacement-controlled (single) loading. The built-in FISH function of the software was invoked in the tests to record the change curves of the upper load with time and meso-fractures. Because the parallel bond model was used in the computation, the model remained certain with regard to the bearing capacity after failure under stress. The test was stopped when the vertical load reached 70% of  $\sigma_{max}$  in the post-peak stage.

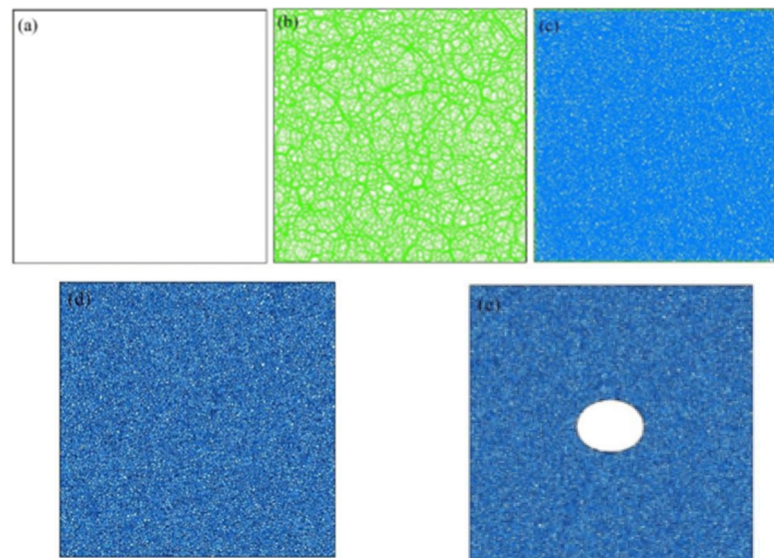


**Figure 9.** Calculation flow of PFC test. (a) Generating boundaries. (b) Setting random seeds. (c) Assigning the mesoscopic parameters. (d) Applying confining pressure (e) Excavation.

#### 4.2. Meso-Fracture Analysis

##### 4.2.1. Evolution of Meso-Fractures

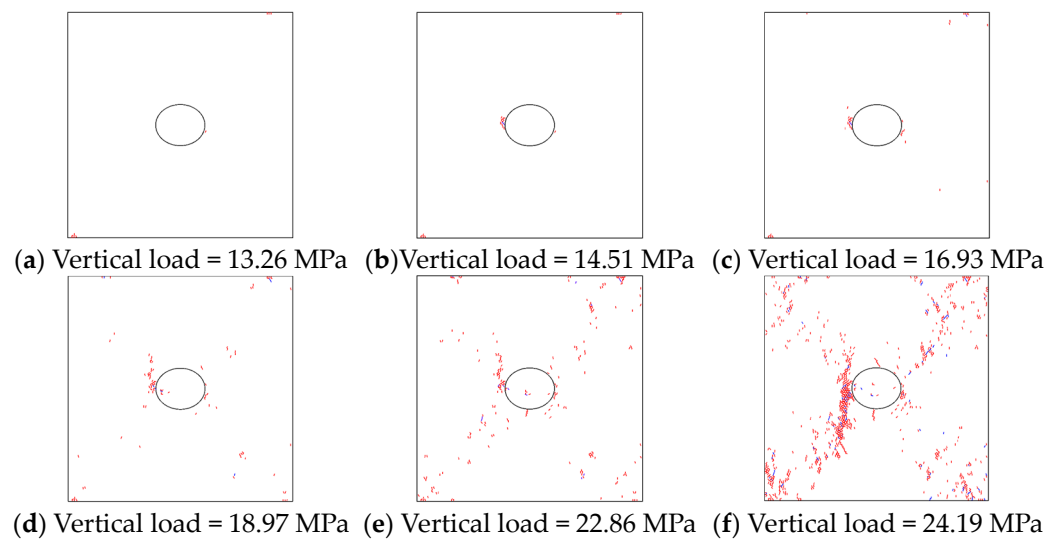
The meso-fracture development process in the loading process was recorded using the built-in FISH language of PFC. Therein, red and blue separately represented tensile and shear fractures. In the meantime, the change curves of the numbers of various types of fractures with the vertical load were recorded so as to analyze the quantitative characteristics of the fractures in the different loading stages.

Figure 10 shows the meso-fracture evolution process recorded in the PFC tests on the elliptical tunnel. The overall bearing capacity of the model is 24.19 MPa, as shown in Figure 8. On this basis, tensile fractures appear on the right side of the tunnel entrance when the vertical load is 13.26 MPa (57.81% of the peak stress; Figure 10a).

When the vertical stress is 14.51 MPa (59.98% of the peak stress; Figure 10b), a small number of fractures are concentrated at the left end of the long axis of the tunnel entrance, and shear fractures begin to appear. Under a vertical stress of 16.93 MPa (69.98% of the peak stress; Figure 10c), the number of meso-fractures on the right side of the entrance increases, and a small number of fractures are initiated at the upper boundary of the model.

When the vertical stress is 18.97 MPa (78.42% of the peak stress; Figure 10d), the number of meso-fractures on the left side of the tunnel entrance increases, and these fractures tend to develop vertically upwards, and a small number of particles drop from the interior of the tunnel on the left side. When the vertical stress is 22.86 MPa (94.50% of the peak stress; Figure 10e), a slender vertical fractured zone is preliminarily formed on the left side of the tunnel and a few particles drop off in the tunnel, while there are only a small number of fractures on the whole. As the load reaches its peak, a vertical fractured

zone with a width of 30 mm and length of 190 mm is formed on the left side of the tunnel, from which particles fall in chunks in the tunnel.



**Figure 10.** Fine-scale fracture evolution in PFC tests in elliptical tunnel (red lines are tension cracks, and blue lines are shear cracks).

Combined with the above results, the fractures around the elliptical tunnel are mainly distributed at one end of the long axis. Under the low load, some fractures concentrate on the left side and tend to propagate upward. As the applied stress increases, a slender vertical fractured zone is preliminarily formed on the left side, from which a few particles drop off in the tunnel. At failure of surrounding rocks, coalesced slender fractures are formed on the left side, and both sides of the tunnel experience spalling.

#### 4.2.2. Types of Fractures and Quantitative Analysis

The change curves of the number of different types of fractures with the vertical load in the PFC tests on the elliptical tunnel are shown in Figure 11.

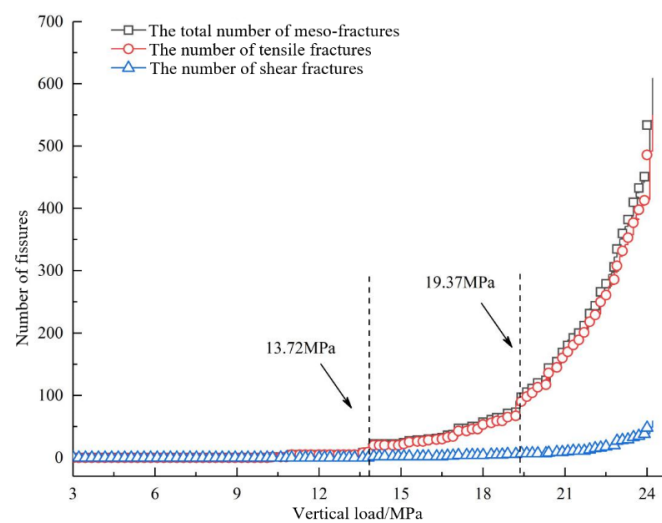


**Figure 11.** Number of meso-cracks–load curve.

- (1) When the vertical stress is 13.72 MPa, the number of tensile fractures and the total number of meso-fractures increase slightly, and the slopes of their curves begin to increase after these changes. In comparison, the shear fractures do not exhibit

significant changes. Under these conditions, tensile fractures begin to initiate at the end of the long axis of the tunnel.

- (2) When the vertical stress is 19.37 MPa, the slopes of the curves of the number of tensile fractures and the total number of meso-fractures increase, while that of the shear fractures slightly increases. This process corresponds to the formation and development of the meso-fractured zone on the left side of the tunnel in the meso-fracture evolution image.
- (3) The number of tensile fractures and the total number of meso-fractures substantially increase when the vertical load reaches its peak, in which the shear fractures only account for 9.69% of the total.

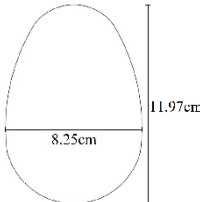
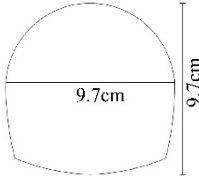
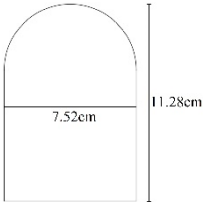
## 5. Simulations of Optimization of the Tunnel Shape

### 5.1. Simulation Schemes

When studying the influence of the tunnel shape on the surrounding rock stability of the tunnel, it was difficult to prepare similar models of tunnels of multiple shapes commonly seen in practice due to the limitations of the preparation techniques. Considering this, PFC simulations were applied to tunnels of different shapes based on the mesoscopic parameters of the elliptical tunnel to explore the failure of rocks surrounding the tunnel and then optimize the shape of a single tunnel.

The main tunnel in underground engineering generally has a U-shaped or straight-walled arched cross-section. However, tunnels of other cross-sectional shapes are also used in traffic, connecting, and water curtain roadways due to the use of different construction methods. To better compare tunnels of different shapes, PFC simulation models of three types of tunnels, namely, egg-shaped, U-shaped, and straight-walled tunnels, were designed following the principle of an equal cross-sectional area as the elliptical tunnel. The dimensions of the model are summarized in Table 2.

**Table 2.** Dimensions of different refuge section models.

Tunnel Shape	Egg-Shaped	U-Shaped	Straight-Walled
Height–span ratio	1.45	1.0	1.5
Cross-sectional area	78.83 mm <sup>2</sup>	78.71 mm <sup>2</sup>	78.76 mm <sup>2</sup>
Dimensions			

### 5.2. Meso-Fracture Evolution

Figure 12 shows the meso-fracture evolution process of models of different tunnels under the same stress paths:

- (1) When the vertical load is 70% of  $\sigma_{zmax}$  in the pre-peak stage, fractures are distributed as thin strips with a length of 60 mm at the arch foot in the lower right part of the egg-shaped tunnel entrance, and they develop obliquely ( $80^\circ$ ) toward the upper right part. Some fractures cut the rocks on the left-side wall, causing the detachment of particles. Fractures around the U-shaped tunnel are mainly concentrated at the spandrel on the right side of the entrance, while the number is small. A V-shaped fracture concentration zone is formed at the right spandrel of the straight-walled arched tunnel entrance, accompanied by the dropping of a small number of particles.
- (2) When the vertical load reaches 80% of  $\sigma_{zmax}$  in the pre-peak stage, many fractures are concentrated in the range of 15 mm in the lower left part of the egg-shaped tunnel, leading to the spalling of the tunnel walls. More fractures appear at the left spandrel of the U-shaped tunnel, accompanied by the dropping of a small number of particles.

- A V-shaped fractured zone is formed in the left spandrel of the straight-walled arched tunnel, where the number of particles spalling from the rock increases.
- (3) When the vertical load is 90% of  $\sigma_{zmax}$  in the pre-peak stage, a triangular fractured zone with a width of 40 mm is formed on the left side of the egg-shaped tunnel, where rocks are exfoliated in chunks. A vertical strip-shaped fractured zone with a width of 20 mm and length of 100 mm is formed on the left-hand side. For the U-shaped tunnel, fractures cut rocks at the left spandrel, resulting in particles dropping off in chunks, and a larger number of fractures appear at the right arch foot. With regard to the straight-walled arched tunnel, fractures at the right spandrel and arch foot coalesce, forming a semicircular fractured area and causing spalling in the tunnel.
  - (4) When the overall load of the model reaches the peak load, symmetric semicircular fractured zones are formed on the left and right sides of the egg-shaped tunnel, with a maximum width of 50 mm. An oblique coalesced fracture with a width of 20 mm and length of 170 mm is initiated at the lower right arch foot of the U-shaped tunnel. Symmetric semicircular fractured zones with a maximum width of 50 mm are also formed on both sides of the straight-walled arched tunnel, from which rocks are exfoliated in chunks.

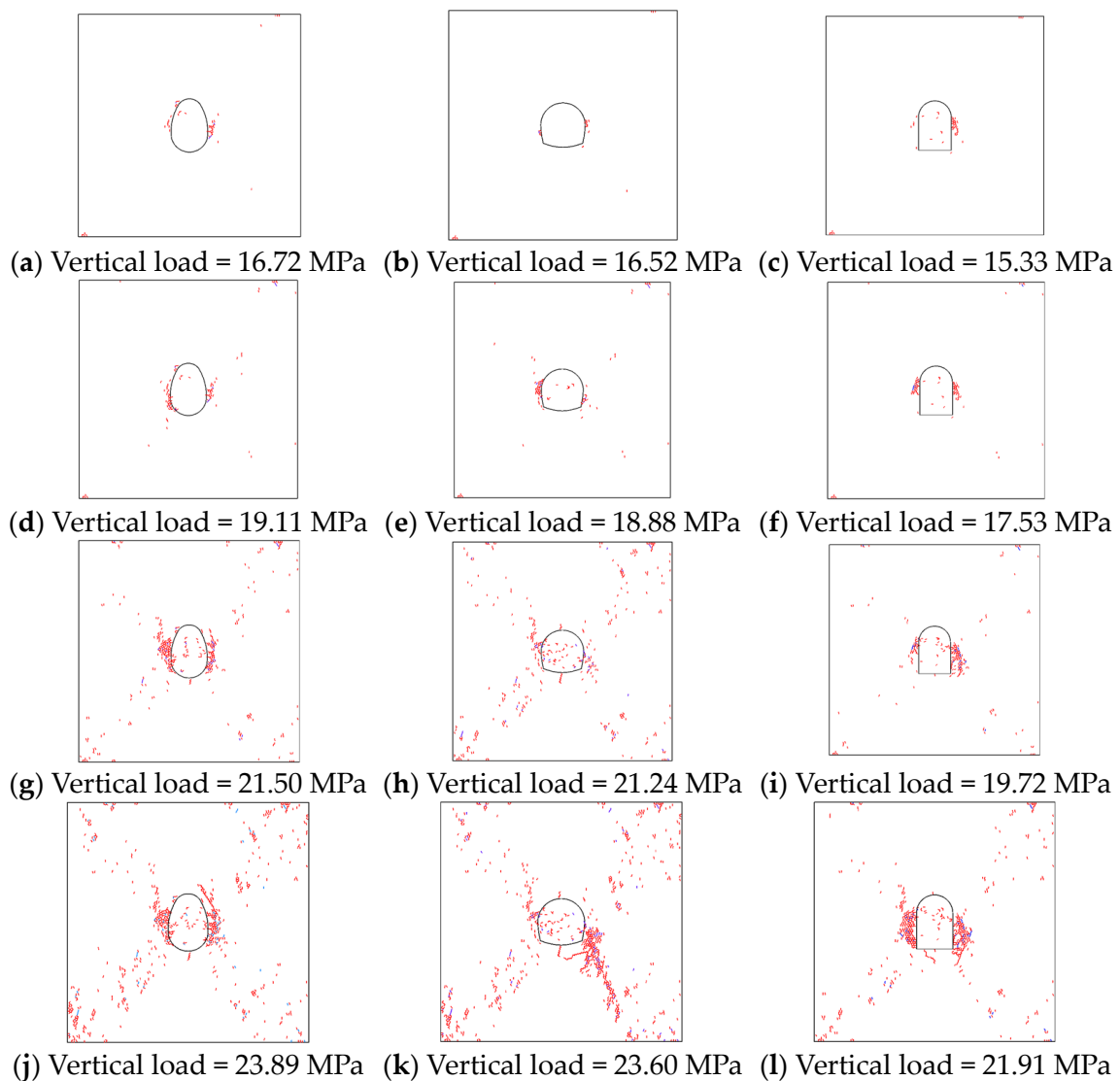
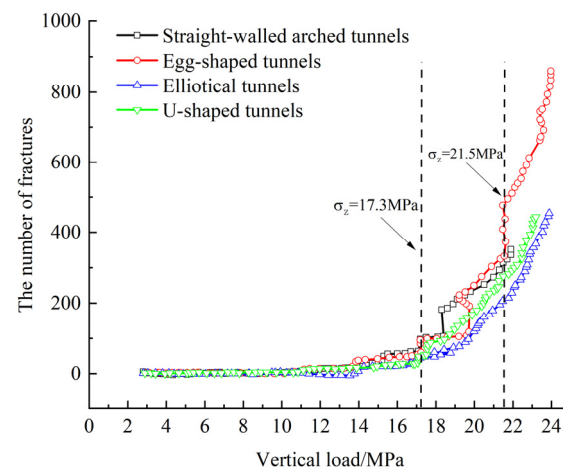


**Figure 12.** Fine-scale fracture evolution of PFC tests for different shapes of tunnels. (Red lines are tension cracks, and blue lines are shear cracks).

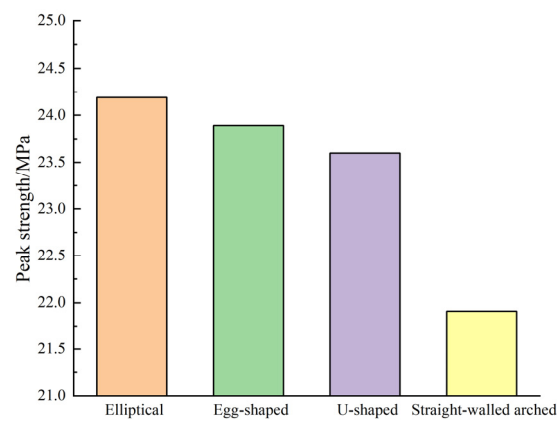
Comparing the above results reveals that under the same load, there are only a few fractures around the U-shaped tunnel, and spalling is insignificant in the tunnel. Rocks are finally damaged because the slender coalesced fractured zone formed in the deep part damages the overall bearing structure, and fractures are mainly distributed at the spandrel and arch foot. There are many fractures around the egg-shaped and straight-walled arched tunnels, along with significant spalling in the tunnels: large areas of fractured zones are formed on both the left and right sides of the two tunnels, where rocks are exfoliated in chunks from the tunnel walls, which finally causes overall failure.

### 5.3. Stress Analysis

The overall peak stresses and force chain distribution in each model were recorded in the test process, as shown in Figures 13 and 14.



(a) Total number of microscopic cracks.



(b) Peak loads for different models.

**Figure 13.** Peak load levels and total number of microscopic cracks for different cross-section chamber models.

Figure 13 shows that the stresses at which fractures increase in the egg-shaped and straight-walled arched tunnels are lower than those of the other two types of tunnels. After the vertical stress reaches 17.3 MPa, the rate of increase in the number of fractures in each model grows. At the same applied load, the different types of tunnels are listed (in descending order) as egg-shaped and straight-walled arched tunnels, U-shaped tunnels, and then elliptical tunnels according to the number of fractures in each model.

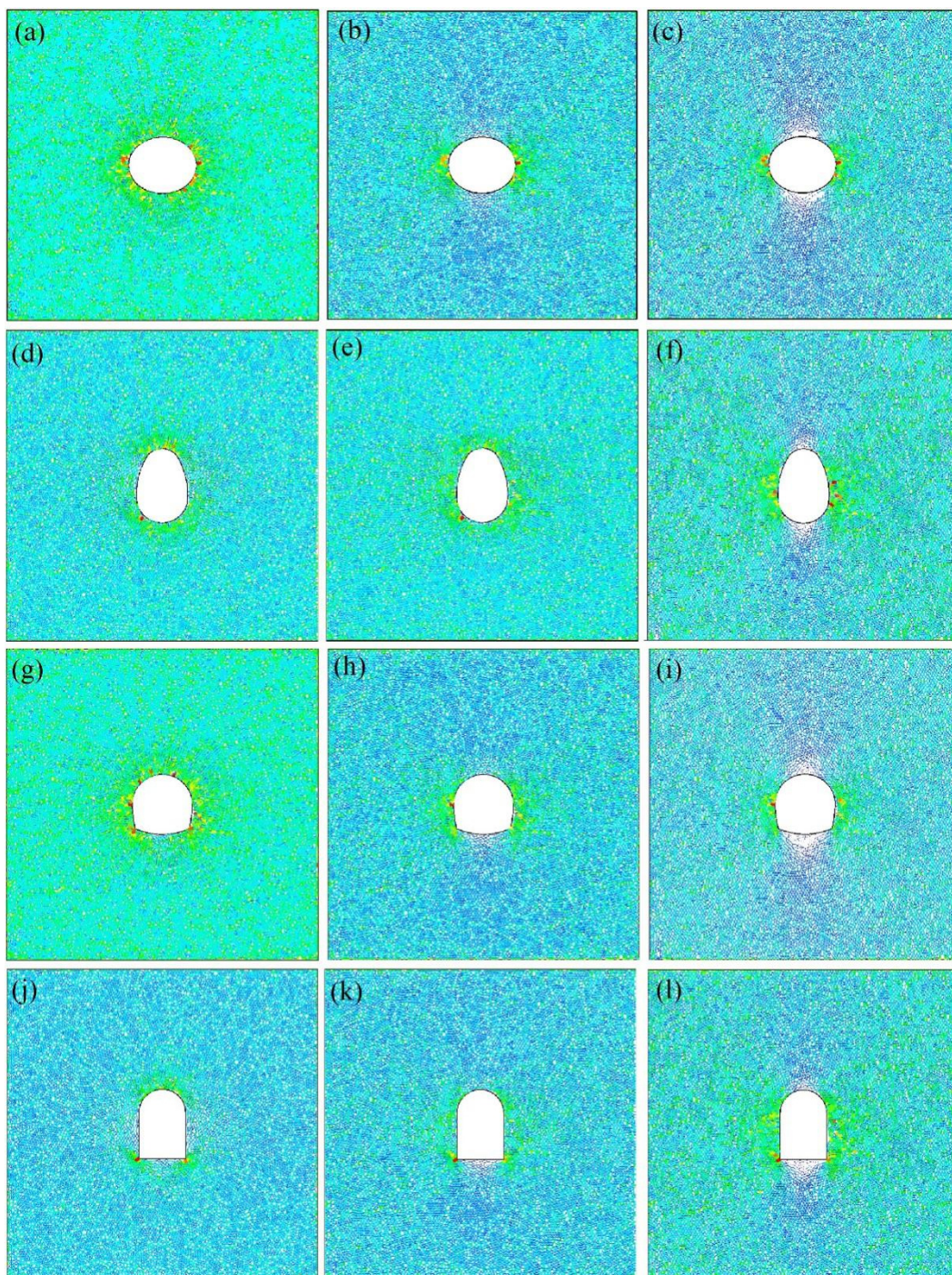


**Figure 14.** Distribution of force chains for different chamber models. ((a–l) represent force chain distributions at 70%, 80%, and 90% of peak strength for the elliptical, egg-shaped, U-shaped, and straight-walled arched models respectively).

Under a vertical stress of 21.5 MPa, the number of fractures in the egg-shaped tunnel model increases suddenly to 480, which is about twice that in the U-shaped tunnel model and 2.5 times that in the elliptical tunnel. The egg-shaped tunnel model shows a higher bearing capacity than the U-shaped and straight-walled arched ones. This is because after the load reaches 90% of  $\sigma_{zmax}$  (21.9 MPa), the stress is transferred to the deep part and forms a temporarily stable bearing structure, which can still bear loads, while fractured zones with the spallation of large rock blocks are formed on both side walls. Under these conditions, accidents are likely to occur in practice.

The various tunnels are listed (in descending order) as elliptical tunnels, egg-shaped tunnels, U-shaped tunnels, and then straight-walled arched tunnels according to their ultimate bearing capacities. If benchmarked against the elliptical tunnel, the peak loads of the egg-shaped, U-shaped, and straight-walled arched tunnels are 98.76%, 97.56%, and 90.57% that of their elliptical counterpart, respectively. The elliptical tunnel has a high ultimate bearing capacity, and those of the egg-shaped and U-shaped tunnels differ slightly, while the ultimate bearing capacity of the straight-walled arched tunnel is much lower than those of the other three. According to results in Figure 13, this phenomenon may occur because stress concentration is likely to appear at the arch feet on both sides of the straight-walled arched tunnel, where the rocks are initially most prone to failure and then influence the stability of the entire bearing structure.

Figure 14 compares the distribution of force chains in the failure process of the various tunnel models. In Figure 14, the vertical loads on the four types of tunnels exert low influences on the upper and lower sides of the tunnel entrances, while stress is significantly concentrated on both the left and right sides of the entrances. Therein, the end of the long axis of the elliptical tunnel shows a significant stress concentration, where force chains are mainly distributed vertically and meso-fractures are first concentrated, finally developing into a vertical fractured zone aligned with the force chains.

Force chains around the U-shaped tunnel are distributed along the tunnel walls. The stresses are high at the arch foot and spandrel, and rocks at the left spandrel show particle clustering and spallation under the high stress. The stress concentration at the right arch foot allows the development of fractures thereat, which finally develop into a slender coalesced fractured zone.

The egg-shaped and straight-walled arched tunnels share similar failure modes and force chain distributions, and their depth–span ratios are both 1.5. Therefore, the tunnel walls have large angles with the force chains, which cause more significant tension to develop in the rocks. In the meantime, due to the high stress level at the spandrel, fractures are concentrated at that position at first, then develop along force chains, and finally coalesce with fractures at the arch foot, thus exfoliating rocks in chunks.

## 6. Discussion

In the field of deep rock engineering, the process of tunnel failure is understood to involve the initiation, propagation, and interaction of cracks, as well as the deformation and damage of surrounding rock, which exhibit characteristics of time evolution [34]. The observed distribution of fractures predominantly at one end of the long axis of elliptical tunnels indicates a unique fracture pattern, primarily characterized by tensile fractures. This finding is consistent with previous studies on tunneling-induced fractures in rock masses. The identification of strain concentration zones on the tunnel surface corresponding to crack initiation and propagation positions underscores the role of strain localization in rock-fracturing processes. This localized strain distribution, as evidenced by the non-uniformity on the tunnel surface, serves as a precursor to macro-crack initiation, propagation, and coalescence. Such insights into strain localization are crucial for understanding the mechanisms governing rock mass behavior under tunneling conditions and can significantly contribute to predictive modeling and risk assessment in tunnel engineering projects. The DIC calculation in this study was limited to considering the phase of strain field continuity. However, following the tunnel failure, the surface becomes discontinuous, resulting in significant errors in strain field calculation. Therefore, this aspect is disregarded. Additionally, the DIC method is only capable of capturing surface crack propagation, while the development of micro-cracks within the sample necessitates the use of alternative detection methods such as acoustic emission.

The comparative analysis of tunnel cross-sections revealed varying peak loads and failure modes, highlighting the influence of tunnel geometry on structural performance. Compared with the test by Cai [35], the strength characteristics of holes with different shapes follow the rule of intact sample > oval sample > U-shaped sample, which is consis-

tent. The bearing capacity of the elliptical cross-section at failure is higher, and the failure of the rock occurs abruptly. Fractured zones are formed on the side walls of tunnels with egg-shaped and straight-walled arched cross-sections, so they cannot give full play to the overall bearing capacity of the rocks. While retaining a certain bearing capacity, the U-shaped cross-section does not exhibit spallation of large rock blocks. Similarly, the initial tensile crack starts at the bottom of the tunnel, but the final failure is the shear failure of the tunnel side wall or spandrel. Zhou [27] used a method of relative displacement between particles in PFC analysis to identify crack types. However, this paper did not establish a quantitative crack identification index and early warning method, which will be further studied in the next work.

## 7. Conclusions

In this study, biaxial loading tests were conducted on elliptical borehole rock samples to study the tunnel rupture evolution process aided by DIC. These processes were tested and simulated by means of a numerical model. The peak strength and failure characteristics of different section shapes under the same section area were discussed. The following conclusions can be drawn:

- (1) Fractures around the elliptical tunnel are found to be mainly distributed at one end of the long axis, and they are mainly tensile fractures. The failure of the elliptical tunnel constructed in sandstone is mainly dominated by slabbing, with the failure mode similar to a V-shaped notch.
- (2) The positions of strain concentration zones on the tunnel surface correspond to the crack initiation and propagation positions. Therefore, strain localization is an important characteristic of rock fracturing, which is shown as the non-uniform distribution of local strain on the tunnel surface.
- (3) During the loading process, the initial crack is a tension crack, which originates from the bottom and top of the tunnel, and then a shear crack appears at the spandrel and the side wall of the tunnel.
- (4) Benchmarked against the elliptical cross-section, the peak loads of tunnels with egg-shaped, U-shaped, and straight-walled arched cross-sections are 98.76%, 97.56%, and 90.57% that of their elliptical counterpart, respectively.

This paper provides biaxial loading test data of large-scale sandstone under graded-loading stress paths, and these observations help us to understand the evolution of tunnel rupture and provide insights for future research in this area to assist in optimizing the excavation and support schemes for underground projects. Further excavation can be carried out in future research into areas such as crack prediction and damage warning.

**Author Contributions:** Conceptualization, S.Q. and Y.C.; methodology, S.Q.; software, L.J.; validation, L.J., Y.C. and X.W.; formal analysis, L.J.; writing—original draft preparation, L.J.; writing—review and editing, L.J., S.Q., Y.C. and X.W. All authors have read and agreed to the published version of the manuscript.

**Funding:** This research was financially supported by the Natural Science Foundation of China (Grant No. 51979268, 52279117). We gratefully acknowledge all the supports of this work.

**Data Availability Statement:** Some or all of the data, models, or code that support the findings of this study are available from the corresponding author upon reasonable request.

**Acknowledgments:** We would like to express our sincere gratitude to those who made efforts in reviewing and editing this article.

**Conflicts of Interest:** The authors declare no conflict of interest.

## References

1. Martino, J.B.; Chandler, N.A. Excavation-induced damage studies at the Underground Research Laboratory. *Int. J. Rock Mech. Min. Sci.* **2004**, *41*, 1413–1426. [[CrossRef](#)]

2. Feng, X.T.; Xu, H.; Qiu, S.L.; Li, S.J.; Yang, C.X.; Guo, H.S.; Cheng, Y.; Gao, Y.H. In Situ Observation of Rock Spalling in the Deep Tunnels of the China Jinping Underground Laboratory (2400 m Depth). *Rock Mech. Rock Eng.* **2018**, *51*, 1193–1213. [[CrossRef](#)]
3. Luo, Y.; Gong, F.Q.; Li, X.B.; Wang, S.Y. Experimental simulation investigation of influence of depth on spalling characteristics in circular hard rock tunnel. *J. Cent. South Univ.* **2020**, *27*, 891–910. [[CrossRef](#)]
4. Zhao, T.B.; Guo, W.Y.; Tan, Y.L.; Yin, Y.C.; Cai, L.S.; Pan, J.F. Case Studies of Rock Bursts Under Complicated Geological Conditions During Multi-seam Mining at a Depth of 800 m. *Rock Mech. Rock Eng.* **2018**, *51*, 1539–1564. [[CrossRef](#)]
5. Yang, X.J.; Ming, W.; Zhang, W.R.; Zhu, C.; Mao, Y.D.; Wang, X.; He, M.C.; Tao, Z.G. Support on Deformation Failure of Layered Soft Rock Tunnel Under Asymmetric Stress. *Rock Mech. Rock Eng.* **2022**, *55*, 7587–7609. [[CrossRef](#)]
6. Gong, F.Q.; Luo, Y.; Li, X.B.; Si, X.F.; Tao, M. Experimental simulation investigation on rockburst induced by spalling failure in deep circular tunnels. *Tunn. Undergr. Space Technol.* **2018**, *81*, 413–427. [[CrossRef](#)]
7. Gong, F.Q.; Si, X.F.; Li, X.B.; Wang, S.Y. Experimental Investigation of Strain Rockburst in Circular Caverns Under Deep Three-Dimensional High-Stress Conditions. *Rock Mech. Rock Eng.* **2019**, *52*, 1459–1474. [[CrossRef](#)]
8. Mazaira, A.; Konicek, P. Intense rockburst impacts in deep underground construction and their prevention. *Can. Geotech. J.* **2015**, *52*, 1426–1439. [[CrossRef](#)]
9. Hajiabdolmajid, V.; Kaiser, P.K.; Martin, C.D. Modelling brittle failure of rock. *Int. J. Rock Mech. Min. Sci.* **2002**, *39*, 731–741. [[CrossRef](#)]
10. Zhong, Z.B.; Deng, R.G.; Lv, L.; Fu, X.M.; Yu, J. Fracture mechanism of naturally cracked rock around an inverted U-shaped opening in a biaxial compression test. *Int. J. Rock Mech. Min. Sci.* **2018**, *103*, 242–253. [[CrossRef](#)]
11. Bai, Q.S.; Tibbo, M.; Nasser, M.H.B.; Young, R.P. True Triaxial Experimental Investigation of Rock Response Around the Mine-By Tunnel Under an In Situ 3D Stress Path. *Rock Mech. Rock Eng.* **2019**, *52*, 3971–3986. [[CrossRef](#)]
12. Wang, S.F.; Huang, L.Q.; Li, X.B. Analysis of rockburst triggered by hard rock fragmentation using a conical pick under high uniaxial stress. *Tunn. Undergr. Space Technol.* **2020**, *96*, 103195. [[CrossRef](#)]
13. Lu, J.; Yin, G.Z.; Gao, H.; Li, X.; Zhang, D.M.; Deng, B.Z.; Wu, M.Y.; Li, M.H. True Triaxial Experimental Study of Disturbed Compound Dynamic Disaster in Deep Underground Coal Mine. *Rock Mech. Rock Eng.* **2020**, *53*, 2347–2364. [[CrossRef](#)]
14. Du, K.; Tao, M.; Li, X.B.; Zhou, J. Experimental Study of Slabbing and Rockburst Induced by True-Triaxial Unloading and Local Dynamic Disturbance. *Rock Mech. Rock Eng.* **2016**, *49*, 3437–3453. [[CrossRef](#)]
15. Mei, S.M.; Feng, X.T.; Li, Z.W.; Yang, C.X.; Gao, J.K. Experimental Study on the Failure Process of Fault Rock Bursts in Tunnels Based on a 3D-Printed Large-Scale Physical Model. *Int. J. Geomech.* **2023**, *23*, 04023139. [[CrossRef](#)]
16. Bobet, A.; Einstein, H.H. Fracture coalescence in rock-type materials under uniaxial and biaxial compression. *Int. J. Rock Mech. Min. Sci.* **1998**, *35*, 863–888. [[CrossRef](#)]
17. Wong, L.N.Y.; Einstein, H.H. Systematic evaluation of cracking behavior in specimens containing single flaws under uniaxial compression. *Int. J. Rock Mech. Min. Sci.* **2009**, *46*, 239–249. [[CrossRef](#)]
18. Cheng, H.; Zhou, X.P.; Zhu, J.; Qian, Q.H. The Effects of Crack Openings on Crack Initiation, Propagation and Coalescence Behavior in Rock-Like Materials Under Uniaxial Compression. *Rock Mech. Rock Eng.* **2016**, *49*, 3481–3494. [[CrossRef](#)]
19. Park, C.H.; Bobet, A. Crack initiation, propagation and coalescence from frictional flaws in uniaxial compression. *Eng. Fract. Mech.* **2010**, *77*, 2727–2748. [[CrossRef](#)]
20. Roux, S.; Réthoré, J.; Hild, F. Digital image correlation and fracture: An advanced technique for estimating stress intensity factors of 2D and 3D cracks. *J. Phys. D-Appl. Phys.* **2009**, *42*, 214004. [[CrossRef](#)]
21. Zhou, X.P.; Zhang, J.Z.; Qian, Q.H.; Niu, Y. Experimental investigation of progressive cracking processes in granite under uniaxial loading using digital imaging and AE techniques. *J. Struct. Geol.* **2019**, *126*, 129–145. [[CrossRef](#)]
22. Zhao, H.G.; Liu, C.; Huang, G.; Yu, B.C.; Liu, Y.B.; Song, Z.L. Experimental investigation on rockburst process and failure characteristics in trapezoidal tunnel under different lateral stresses. *Constr. Build. Mater.* **2020**, *259*, 119530. [[CrossRef](#)]
23. Zhang, L.W.; Fu, H.; Wu, J.; Zhang, X.Y.; Zhao, D.K. Effects of Karst Cave Shape on the Stability and Minimum Safety Thickness of Tunnel Surrounding Rock. *Int. J. Geomech.* **2021**, *21*, 15. [[CrossRef](#)]
24. Tang, Y.; Okubo, S.; Xu, J.; Peng, S.J. Progressive failure behaviors and crack evolution of rocks under triaxial compression by 3D digital image correlation. *Eng. Geol.* **2019**, *249*, 172–185. [[CrossRef](#)]
25. Yang, S.Q.; Yin, P.F.; Zhang, Y.C.; Chen, M.; Zhou, X.P.; Jing, H.W.; Zhang, Q.Y. Failure behavior and crack evolution mechanism of a non-persistent jointed rock mass containing a circular hole. *Int. J. Rock Mech. Min. Sci.* **2019**, *114*, 101–121. [[CrossRef](#)]
26. Zhang, K.; Zhang, K.; Bao, R.; Fan, W.C.; Xie, J.B. A novel quantitative explanation for the fracture mechanism of sandstone containing a circular inclusion. *Fatigue Fract. Eng. Mater. Struct.* **2023**, *46*, 1775–1791. [[CrossRef](#)]
27. Zhou, Z.L.; Tan, L.H.; Cao, W.Z.; Zhou, Z.Y.; Cai, X. Fracture evolution and failure behaviour of marble specimens containing rectangular cavities under uniaxial loading. *Eng. Fract. Mech.* **2017**, *184*, 183–201. [[CrossRef](#)]
28. Chen, Y.; Zuo, J.P.; Li, Z.H.; Dou, R. Experimental investigation on the crack propagation behaviors of sandstone under different loading and unloading conditions. *Int. J. Rock Mech. Min. Sci.* **2020**, *130*, 104310. [[CrossRef](#)]
29. Aydin, G. Recycling of abrasives in abrasive water jet cutting with different types of granite. *Arab. J. Geosci.* **2014**, *7*, 4425–4435. [[CrossRef](#)]
30. Aydin, G.; Kaya, S.; Karakurt, I. Effect of abrasive type on marble cutting performance of abrasive waterjet. *Arab. J. Geosci.* **2019**, *12*, 1–8. [[CrossRef](#)]
31. Pan, B. Recent Progress in Digital Image Correlation. *Exp. Mech.* **2011**, *51*, 1223–1235. [[CrossRef](#)]

32. Pan, B.; Qian, K.M.; Xie, H.M.; Asundi, A. Two-dimensional digital image correlation for in-plane displacement and strain measurement: A review. *Meas. Sci. Technol.* **2009**, *20*, 062001. [[CrossRef](#)]
33. Gao, K.; Harrison, J.P. Scalar-valued measures of stress dispersion. *Int. J. Rock Mech. Min. Sci.* **2018**, *106*, 234–242. [[CrossRef](#)]
34. Bao, H.; Liu, C.Q.; Liang, N.; Lan, H.X.; Yan, C.G.; Xu, X.H. Analysis of large deformation of deep-buried brittle rock tunnel in strong tectonic active area based on macro and microcrack evolution. *Eng. Fail. Anal.* **2022**, *138*, 106351. [[CrossRef](#)]
35. Cai, X.; Yuan, J.F.; Zhou, Z.L.; Pi, Z.Z.; Tan, L.H.; Wang, P.Y.; Wang, S.Y.; Wang, S.F. Effects of hole shape on mechanical behavior and fracturing mechanism of rock: Implications for instability of underground openings. *Tunn. Undergr. Space Technol.* **2023**, *141*, 105361. [[CrossRef](#)]

**Disclaimer/Publisher’s Note:** The statements, opinions and data contained in all publications are solely those of the individual author(s) and contributor(s) and not of MDPI and/or the editor(s). MDPI and/or the editor(s) disclaim responsibility for any injury to people or property resulting from any ideas, methods, instructions or products referred to in the content.